The Meteoritical Society

Meteoritics & Planetary Science 54, Nr 1, 181–201 (2019)
doi: 10.1111/maps.13184

Shock metamorphic history of >4 Ga Apollo 14 and 15 zircons

Carolyn A. CROW[1,2*], Desmond E. MOSER[3], and Kevin D. McKEEGAN[4]

[1]Nuclear and Chemical Sciences Division, Lawrence Livermore National Laboratory, Livermore, California 94550, USA
[2]Department of Geological Sciences, University of Colorado, Boulder, Colorado 80309, USA
[3]Zircon and Accessory Phase Laboratory, University of Western Ontario, London, Ontario N6A 5B7, Canada
[4]Department of Earth, Planetary, and Space Sciences, University of California, Los Angeles, Los Angeles, California 90095, USA
[*]Corresponding author. E-mail: carolyn.crow@colorado.edu

(Received 08 August 2017; revision accepted 29 June 2018)

Abstract–During impact events, zircons develop a wide range of shock metamorphic features that depend on the pressure and temperature conditions experienced by the zircon. These conditions vary with original distance from impact center and whether the zircon grains are incorporated into ejecta or remain within the target crust. We have employed the range of shock metamorphic features preserved in >4 Ga lunar zircons separated from Apollo 14 and 15 breccias and soils in order to gain insights into the impact shock histories of these areas of the Moon. We report microstructural characteristics of 31 zircons analyzed using electron beam methods including electron backscatter pattern (EBSP) and diffraction (EBSD). The major results of this survey are as follows. (1) The abundance of curviplanar features hosting secondary impact melt inclusions suggests that most of the zircons have experienced shock pressures between 3 and 20 GPa; (2) the scarcity of recrystallization or decomposition textures and the absence of the high-pressure polymorph, reidite, suggests that few grains have been shocked to over 40 GPa or heated above 1000 °C in ejecta settings; (3) one grain exhibits narrow, arc-shaped bands of twinned zircon, which map out as spherical shells, and represent a novel shock microstructure. Overall, most of the Apollo 14 and 15 zircons exhibit shock features similar to those of terrestrial zircon grains originating from continental crust below large (~200 km) impact craters (e.g., Vredefort impact basin), suggesting derivation from central uplifts or uplifted rims of large basins or craters on the Moon and not high-temperature and -pressure ejecta deposits.

INTRODUCTION

The crystal structures of minerals experience deformation and modification unique to shock metamorphism (e.g., French 1968; Stöffler and Hornemann 1972; Stöffler and Langenhorst 1994) and zircon ($ZrSiO_4$) is no exception (El Goresy 1965; Krogh et al. 1984; Timms et al. 2018). Zircon exhibits a variety of crystalline microstructures and textures depending on variables such as the pressure and temperature conditions experienced during impact cratering events. Of particular importance is the duration of exposure to the extreme, high-temperature conditions following the passage of the shock wave, as examined in detail for zircons found in ejecta, impact breccias, and suevite from Ries crater (Germany), Popigai crater (Siberia), Chicxulub crater (Mexico), Mistasin Lake crater (Canada), and Acraman crater (Australia) (e.g., Wittmann et al. 2006; Timms et al. 2017). Some, though not all, impact environments promote accelerated out-diffusion of preimpact, radiogenic Pb or its quantitative removal through mineral recrystallization resulting in partial to complete resetting of the U-Pb chronometer. The latter has been observed in zircons hosted in ultrahigh-temperature ejecta material (e.g., Krogh et al. 1993) and zircons in target rocks beneath impact melt sheets (Moser et al. 2011). Specific shock microstructures allow for broad reconstruction of the shock metamorphic pathway(s) experienced by a given zircon grain and thus can yield insight into the shock

environments experienced by planetary crustal rocks. This is of particular value in reconstructing the impact history of the Moon where samples of the crust have been subject to multiple impacts including large basin-forming events (e.g., Turner et al. 1973; Schaeffer and Husain 1973; Tera et al. 1974; Dalrymple and Ryder 1996; Hartmann 1975, 2003; Ryder 1990; Grange et al. 2013b; Cavosie et al. 2015a).

In this study, we have characterized the shock microstructures in 31 lunar zircons from Apollo 14 and 15 samples by using a combination of secondary electron imaging, cathodoluminescence (CL), and electron backscatter pattern (EBSP) and diffraction (EBSD) analyses. This inventory of lunar zircon shock microstructures is informative as to the pressure and temperature conditions experienced by the Apollo 14 and 15 samples, which can help elucidate their provenance and provide context for measured U-Pb ages of these grains.

OVERVIEW OF SHOCK MICROSTRUCTURES IN ZIRCON

With the increasing attention to zircon as a shock recorder it is becoming apparent that, in the large complex craters on Earth, shock metamorphic features can be divided into two broad classes depending on whether the grains are from the upper "crater and ejecta" facies, or from the deeper target region beneath the impact melt sheet and crater floor that are later exhumed as part of the central uplift (e.g., Moser et al. 2011; Erickson et al. 2013b; Cavosie et al. 2015b; Davis 2017; Timms et al. 2017). Within zircons from both these environments it is common to observe multiple sets of parallel, "crystallographically oriented cracks" at high angles to the c-plane. These microstructures were first identified in natural samples by Krogh et al. (1984) and are similar to the "microcleavage" cracks produced in shock experiments (Leroux et al. 1999), which are now widely recognized in zircons from terrestrial impacts (Corfu et al. 2003). Pervasive crystal-plastic deformation (CPD) of the zircon lattice also appears to be common in zircons that experience a wide range of pressure and temperature conditions covering both natural craters (e.g., Reimold et al. 2002; Moser et al. 2011) and laboratory experiments (Leroux et al. 1999; Morozova et al. 2017). Nevertheless, many shock metamorphic features are distinct to either upper level/ejecta or deep level crater environments.

The distinct features in upper level crater zircon are known from terrestrial samples of impact glass, breccia, suevite, shallow crust at the crater rim, and rapidly cooled impact melt in dykes of pseudotachyllite and granophyre in the crater floor. Zircon decomposition to baddeleyite and pure SiO_2 within rapidly shocked, superheated (>1700 °C) and quenched ejecta facies was first described in impact glass from the Ries and Aouelloul craters (El Goresy 1965; see supporting information for overview of terrestrial impact craters). Later work on K-P distal ejecta (65 Ma) documented a very fine "granular" zircon texture due to conversion of a single grain to an aggregate of thousands of very fine (submicron) neoblasts (Bohor et al. 1993; Krogh et al. 1993), and this was seen again in granophyre dykes injected into the central uplift of the Vredefort impact crater (Kamo et al. 1996). Lamellar and granular domains of the high-pressure polymorph reidite are also diagnostic of impact shock metamorphism (Glass and Liu 2001; Wittmann et al. 2006), as are zircon granules in orientations indicating reversion from reidite such as those seen in the rim of Barringer (a.k.a. Meteor) crater (Cavosie et al. 2016). Overall the distinguishing features of upper crater zircons are phase transformations and chemical breakdown coupled with very fine recrystallization of the original grain; the small grain sizes indicate that these transformations occur over very short time spans. Zircons can preserve these characteristics in ejecta deposited thousands of kilometers from the crater (Krogh et al. 1993).

Zircon shock features in samples of the crystalline crust beneath a crater were first described in a study of Archean gneisses underlying the Sudbury impact melt sheet (Krogh et al. 1984). At Sudbury, the initial radial distance of the samples from impact center is uncertain due to the tectonic reconfiguration of the impact basin. More detailed investigations of zircons from a central uplift were carried out at the deeply eroded (8 to 10 km below the impact basin floor) and undeformed Vredefort structure (Gibson and Reimold 2008). Zircon microstructures similar to those at Sudbury were found in bedrock samples (Kamo et al. 1996; Moser 1997), as well as a distinct coarser (~10 μm) granular texture or "polycrystalline aggregate" (Moser 1997). Crystal-plastic deformation and "mosaicism" were later revealed in a Vredefort central uplift zircon (Reimold et al. 2002) and were confirmed as common shock metamorphic features across a ~50 km diameter area of the impact structure (Moser et al. 2011). Other novel features such as shock microtwin lamellae in {112} orientation were identified in the same zircon population.

The most distinctive and ubiquitous shock microfeatures in the lower crater, however, are the "curviplanar features" decorated by secondary inclusions of impact melt (Moser et al. 2011). These enigmatic microstructures appear to have been a type of short-lived fracture or network of closely spaced fractures, which generally offset grain features at a ~45° angle to the c-axis (i.e., perpendicular to planes of

maximum shear stress as described in Timms et al. 2012; Morozova et al. 2017). These are not to be confused with the open, extensional fractures generated in the ballistic experiments of Leroux et al. (1999), or "nonplanar fractures" described by Timms et al. (2012). Instead, these features are annealed fractures or fracture networks that are materially continuous in secondary electron images of polished surfaces (i.e., no void space) and only observable in BSE, EBSD, and CL imaging. In some samples, there is evidence of trace element alteration of the adjacent zircon based on variations in CL emission. These annealed features accommodate some of the largest strains (microns of offset) and are frequently decorated with μm-scale ovoid to elongated secondary inclusions of silicate material equivalent to the composition of host minerals (Moser et al. 2011; Davis 2017). The inclusions are interpreted as locally derived shock-melts injected during the decompression melting phase of shock wave unloading (Moser et al. 2011; Davis 2017). There was evidence in the first reports that curviplanar features formed prior to microtwin lamellae, before shock wave rarefaction (Moser et al. 2011), although it is now apparent that curviplanar features are often the last shock features to form (Erickson et al. 2013a, 2013b). Current understanding suggests these features are unique to the basement of central uplifts in large impact structures such as Vredefort, which have been recognized as valuable analogs for lunar crust (Gibson et al. 2002).

Zircons separated from Apollo breccias and soils are among some of the oldest dated samples on the Moon (e.g., Nemchin et al. 2008, 2009a, 2009b; Grange et al. 2009, 2011, 2013b; Taylor et al. 2009; Barboni et al. 2017; Crow et al. 2017a) and, as such, they potentially retain a detailed record of the era of basin-forming impact events on the early Moon (Smith et al. 1986; Pidgeon et al. 2007; Nemchin et al. 2008; Grange et al. 2009; Liu et al. 2012; Grange et al. 2013a; Norman and Nemchin 2014; Hopkins and Mojzsis 2015; Bellucci et al. 2016; Crow et al. 2017a). Shock microstructures have been documented in lunar zircons, but the degree of associated Pb-loss is variable among grains with similar deformation features (e.g., Timms et al. 2012; Grange et al. 2013a, 2013b). The main shock microstructures reported so far overlap with those common to terrestrial samples, specifically crystallographically controlled planar features and shock microtwin lamellae (Timms et al. 2012), as well as random fracturing (e.g., the "cracker" grain of Grange et al. 2011). Unusual textures have also been reported, such as brecciated zircon in a "cement" of high-U zircon in the "pomegranate" zircon that dates between ~4.1 and 4.2 Ga (Pidgeon et al. 2007; Bellucci et al. 2016). With regard to inclusions, secondary melt inclusions spatially associated with planar or curviplanar fracturing have only recently been recognized (Crow et al. 2017a). Inclusions in Apollo 14 zircons have also been identified by Nemchin et al. (2008); however, it is unclear if these are primary or secondary in nature. Textures indicative of exposure to prolonged high temperatures, such as recrystallized domains and decomposition to ZrO_2 and SiO_2, have been documented in a small subset of zircons (Grange et al. 2013b; Crow et al. 2017a).

SAMPLE DESCRIPTIONS

Our survey includes a subset of Apollo lunar zircons whose age and petrogenesis were discussed in Crow et al. (2017a). The zircons were separated from two soil samples (14259 and 15311) and two breccia samples (14305 and 14321). Both soil samples were collected from the top few centimeters of the loose regolith on the lunar surface. Soils within the top millimeter of the lunar regolith are exposed to micrometeorites and solar wind, which produce nanophase iron (I_s) (Morris 1978). The concentration of nanophase iron relative to the bulk iron oxide content (I_s/FeO) is therefore an indicator of the soil maturity, or residence time in the top ~1 mm of regolith. Soil 14259 is a mature surface sample (I_s/FeO = 85) (von Engelhardt et al. 1972; McKay et al. 1972; Morris 1978), and zircons from this soil yield ^{207}Pb-^{206}Pb ages between 3.92 and 4.34 Ga (Crow et al. 2017a). Interestingly, a few zircons and agglutinates from this soil show evidence of Pb-loss within the last ~150–600 Myr (Church et al. 1976; Crow et al. 2017a). Soil 15311 (I_s/FeO = 48) was collected from the edge of the small, ~100 m diameter, Spur Crater (Morris 1978). Zircons separated from this soil have ages ranging from 4.25 to 4.36 Ga (Crow et al. 2017a). Crystalline matrix breccia 14305 has relatively high concentrations of clasts within a crystalline matrix; it was collected in the Fra Mauro Formation. Previous studies have reported zircons from 14305 with ages ranging from 3.97 to 4.35 Ga (Hinton and Meyer 1991; Nemchin et al. 2008; Taylor et al. 2009). Sample 14321 is a clast-rich, crystalline matrix breccia also from the Fra Mauro Formation and was collected from the rim of Cone Crater. Zircons from this sample show a wide range of ^{207}Pb-^{206}Pb ages from 3.89 to 4.40 Ga (Meyer et al. 1996; Nemchin et al. 2006, 2008; Taylor et al. 2009). Analyses of Hf isotopes of zircons from 14321 suggest KREEP reservoir formation between 4.478 ± 0.046 Ga and 4.51 ± 0.01 Ga (1σ) (Taylor et al. 2009; Barboni et al. 2017). For a full description of sample, see Crow et al. (2017a) and the Lunar Sample Compendium (https://curator.jsc.nasa.gov/lunar/lsc).

ANALYSES

Sample Preparation

Zircons were separated from lunar breccia and soil samples by crushing, standard heavy liquid (methylene iodide) density separation, and hand picking under an optical microscope aided by ultraviolet light (see Crow et al. 2017a). Zircons were positively identified by energy-dispersive X-ray spectroscopy (EDS) on the UCLA Tescan scanning electron microscope (SEM). The samples were then mounted in 1 inch epoxy rounds, polished with successively finer silicon carbide papers, and finished with a 0.5 μm alumina slurry on a Vibromet automatic polisher for 45 min (following the procedures used in Moser et al. 2011). For most of the samples, this procedure removed surface scratches; however, surface defects remained for a few grains. The last step prior to SEM analyses was to coat the samples with a thin layer of carbon to reduce sample charging that interferes with electron imaging.

Electron Beam Analyses

We collected SEM micrographs and electron backscatter pattern (EBSP) spot measurements for 31 lunar zircons following the analytical methods outlined in Moser et al. (2011). We also collected larger EBSD maps for a subset of seven zircons that contained complex microstructures such as offsetting shock microtwins. We used the Hitachi SU6600 field emission gun (FEG)-SEM in the Zircon and Accessory Phase Laboratory (ZAPLab) at the University of Western Ontario for SEM analyses. Secondary electron (SE) and backscatter electron (BSE) images were collected using a 5 kV accelerating voltage. The relatively low voltage can produce channeling from the lattice planes that most efficiently diffract electrons thereby accentuating any variations in crystallographic orientation. This type of image is, therefore, useful in identifying samples for further EBSD imaging.

Cathodoluminescence (CL) images were collected with the ZAP lab customized Gatan Chroma CL detector and the UCLA Tescan Color CL detector. Both detectors have three channels: red (620–750 nm), green (495–570 nm), and blue (450–495 nm); the Chroma is also equipped with a UV channel (380–450 nm). The rare earth elements (REE) are commonly incorporated into zircons during crystallization and are known to fluoresce when exposed to an electron beam. The emitted radiation from the excited REEs is typically between ~400 nm and 900 nm (e.g., Blanc et al. 2000; Lenz and Nasdala 2015; Tsuchiya et al. 2015). The heavier REEs (e.g., Dy, Er), which are more compatible in the zircon structure, emit mostly in the UV and visible wavelengths with minor emission bands at longer wavelengths. We, therefore, present CL images as summed intensity images across all wavelengths.

The first step of sample characterization involved comparison of the low kV BSE, CL, and conventional higher voltage (15–20 kV) BSE images to identify potential structural and chemical variations. All features observed during initial imaging were spot analyzed (EBSP) to determine if the features were associated with variations in orientation or band contrast. The results of the spot analyses were then used to define targets for further, time intensive, EBSD maps.

A higher accelerating voltage of 20 kV was used for EBSD analyses, and the mount was tilted at a 70° angle relative to the detector and positioned at a working distance of 19.0 mm. This orientation results in a ~50 nm equivalent spot size or interaction volume. To produce EBSD maps, a grid of EBSPs was collected in ~125 nm steps across the sample surface. The mean angular deviation (MAD), or the angle between the measured EBSP and the reference Kikuchi bands for a given mineral phase (Hazen and Finger 1979), was set to 1.7° as an accuracy threshold based on laboratory experience. If the MAD was higher than this value, the EBSD software (Oxford HKL Channel 5) did not index the EBSP and the step was excluded when producing the EBSD map (black pixels in maps). The angular resolution (noise level) for orientation differences between pixels is a maximum of 0.5° ± 0.2 and can be as low as 0.2° ± 0.1 for very highly polished specimens (see supporting information for EBSD analysis parameters). The software was set up to index for zircon, baddeleyite, and reidite; in the cases of adjacent mineral phases, these phases were added to the software indexing. The EBSP data can be quantified by multiple parameters including Kikuchi band contrast (crispness of diffraction pattern), crystallographic orientation, and misorientation relative to a reference point. The grid of EBSP analyses is used to create a map of these parameters that can be compared with CL and low kV BSE images.

RESULTS

The 31 lunar zircons included in our survey range from ~50 to 300 μm in size and mostly between 4.21 Ga and 4.38 Ga in minimum crystallization age (Crow et al. 2017a); four grains have ^{207}Pb-^{206}Pb ages <4.2 Ga. The fact that CL zonation is generally truncated at grain margins suggests that they are fragments of larger crystals. In this way, the zircons often resemble other lunar soil grains, which have sharp shard-like forms, presumably due to repeated impact bombardment.

Some of the lunar zircons have primary growth zoning characteristic of igneous grains, and most show evidence of deformation. Many of the microstructures previously reported for both terrestrial and lunar shock metamorphosed zircons were observed as well as novel features. Below is a summary of each class of textures identified ranging from pristine state to high levels of shock metamorphism.

Homogeneous Zircons

Five zircons in the suite are featureless in that they do not show any evidence of primary magmatic zoning or secondary shock microstructures on the external or polished surfaces (Table 1). Lattice orientation mapping of these grains with EBSD or EBSP did not reveal the existence of annealed fractures or impact melt inclusions. Breccia zircon 14321 Z14 is one of the best examples of this type of grain. SEM images of this ~300 μm grain suggest that it is compositionally and structurally homogeneous (Figs. 1A and 1B) (Crow et al. 2017a). EBSD analyses also show that the grain is structurally homogeneous with <0.7° of variation in crystal orientation (Fig. 1C). Seven REE and Ti analyses reported in Crow et al. (2017a) confirm the homogeneity in trace element compositions.

Primary Igneous Zoning

Primary oscillatory and sector zoning was identified in 13 lunar zircons (~38%; Table 1) based on variations in CL emission. Breccia zircon 14305 Z27 exhibits well-preserved primary oscillatory zoning (Fig. 2A) and a CL dark core (likely due to higher U concentration) surrounded by a brighter oscillatory-zoned overgrowth. EBSD point analyses show that the bright outer growth zone is epitaxial; however, there is a slight change in electron diffraction intensity between the core and rim likely due to differences in metamictization, or polishing differences between zones of varying radiation damage. The CL image of zircon 14305 Z29 reveals well-preserved sector zoning (Fig. 2B). Similar to Z27, EBSD line scans show no variation in crystallographic orientation across the sector zoning and a slight reduction in band contrast for the dark CL region. We note that previous U-Pb age analyses of lunar zircons with primary growth zoning show no variation in age between the zones (e.g., Grange et al. 2013a, 2013b; Crow et al. 2017a).

Planar and Curviplanar Features, and Impact Melt Glass Inclusions

Curviplanar features hosting impact melt inclusions are the most prevalent shock microstructures observed in this survey (~67% of zircons; Table 1). These inclusions do not produce EBSP, and the morphology of the inclusions is similar to those in zircons from the Vredefort impact structure, which are ostensibly amorphous. The melt inclusions are not zirconium-silicate and exhibit a range in composition in line with common minerals (see discussion below). We found a wide range in linear and curviplanar features and impact melt properties in the lunar zircons; the following describes the most common morphologies of these features (Fig. 3).

The smallest impact melt inclusions observed in this study were found in breccia zircon 14305 Z15, most of which are well below 1 μm in diameter (Fig. 3A). The inclusions, which do not produce EBSPs, are grouped in multiple sets of linear and curviplanar chains that are easily identifiable in the BSE images, and there is no variation in CL intensity associated with these small inclusions. Breccia zircon 14305 Z36 contains intermediate-sized impact melt inclusions, some of which are up to ~2–3 μm in diameter (Fig. 3B). The material surrounding the inclusions indexes as zircon in EBSD analyses (Fig. 4) but appears bright in low kV BSE and dark in CL. The dark CL response along curviplanar features could be due to altered trace element composition near the fracture (Moser et al. 2011). Zircon 14321 Z10 represents the other endmember in which long segments of impact melt, up to ~60 μm in length, fill a fracture that offsets primary zonation and appears dark in CL. The opposite response (i.e., dark in low kV BSE and bright in CL) was observed around impact melt inclusions in other samples such as 14305 Z25 and Z30 (see the Granular Recrystallization and the Crystal-Plastic Deformation sections). Annealing of zircon has been shown to correlate with an increase in CL emission, so the bright CL behavior would be consistent with annealing of fractures after injection of impact melt (Tsuchiya et al. 2015). The CL response does not appear to be correlated with factors such as inclusion size, primary zoning, or other impact related features.

Breccia zircon 14321 Z12 is a unique sample in that its inclusions appear to have devitrified. The morphology of the inclusions is similar to the previously described samples, ovoid and linearly aligned; however, these inclusions contain euhedral submicron crystals (Fig. 3D). The crystals are too small or insufficiently polished to be reliably identified chemically (EDS) or indexed by phase (EBSD). The chain of inclusions is also associated with bright and dark domains tens of nanometers in diameter in the zircon matrix as seen in the low kV BSE and SE images (e.g., Fig. 3D). These also are too small to reliably index with EBSD, although two pixels indexed as baddeleyite (MAD = 0.7).

Table 1. Inventory of shock microstructures.

Sample	CL zonation[b]	Shock microtwins	Curviplanar fracture	Melt inclusions	Crystal plastic deformation	Amorphous zircon	Shock twins	Recrystallization	Pb-Pb[c] age (Ma)	1σ	Related Fig.
14259 *Soil*											
Z8	O/D		X	X					4336	12	
Z9	S										
Z10											
Z12	S/D				X[a]				4306	4	
Z13									4268	15	
Z14			X	X					4009	12	
14304 *Breccia*											
Z16[d]		X	X	X	X		X		4246	26	Fig. 5
14305 *Breccia*											
Z15			X	X					4206	16	Fig. 3
Z22	S/D		X	X					4219	11	
Z23			X						4332	4	
Z25	O/S/D		X	X	X[a]				4265	5	Fig. 9
Z27	O		X	X					4335	13	Fig. 2
Z29	S								4254	6	Fig. 2
Z30	D		X	X	X			X			
Z31			X	X					4334	5	
Z33					X[a]				4334	4	
Z34	O	X	X	X	X		X		4324	5	Fig. 7
Z36		X	X	X	X[a]		X		4281	5	Fig. 3 & 4
Z42			X	Possible							
14321 *Breccia*											
Z10	S		X	X					4281	38	Fig. 3
Z11	O		X	X					4385	4	
Z12			X	X					4164	3	Fig. 3
Z14									4190	42	Fig. 1
Z17									4097	2	
Z19			X	X					4408	3	
Z20		X	X	X	X	X	X		4241	5	
Z21									4286	6	
15311 *Soil*											
Z3	O		X	X							
Z5	S			X					4373	31	
Z6			X	X	X	X			4301	6	Fig. 6
Z7	O/S/D		X	X					4338	4	

[a]Banded deformation.
[b]O = oscillatory zoning; S = sector zoning; D = diffuse pattern.
[c]Ages are from Crow et al. (2017a, 2017b).
[d]Age is from Taylor et al. (2009).

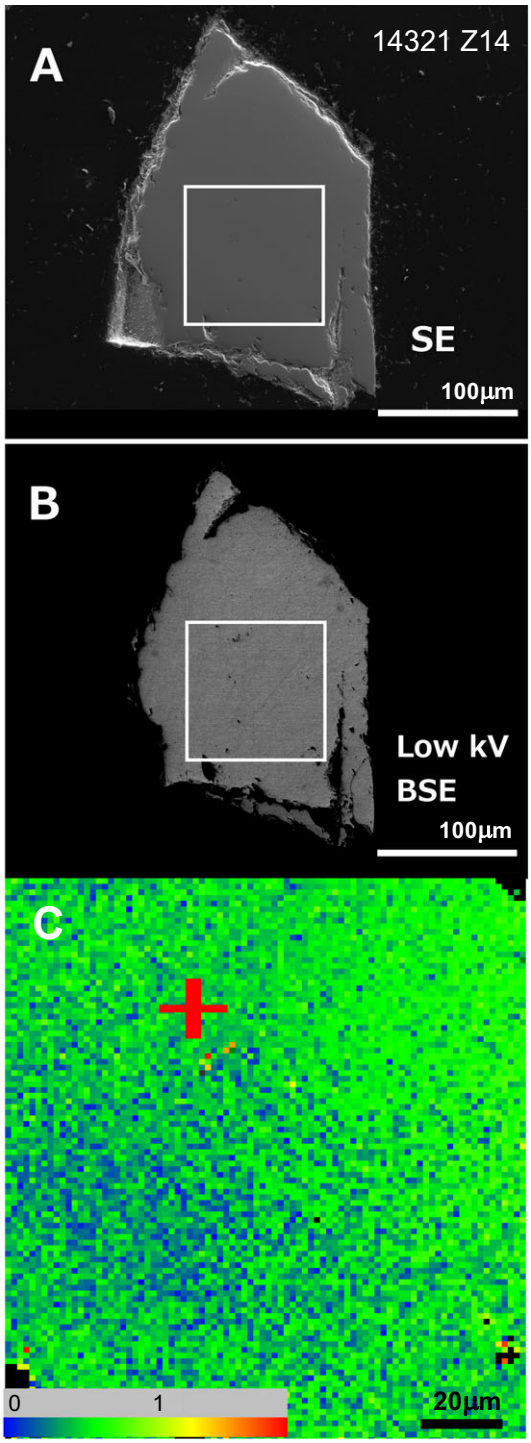

Fig. 1. SEM and EBSD images of a polished section of a representative homogeneous zircon 14321 Z14 (^{207}Pb-^{206}Pb age 4190 ± 42 Ma; Table 1). A) SE image shows no curviplanar features or secondary melt inclusions exposed on the surface. B) Low kV BSE image reveals no variations in composition or structure. Location of EBSD analyses designated with white box. C) EBSD misorientation map relative to red cross reveals <0.7° (detection limit) variation across the grain indicating a single, undeformed lattice at this resolution. (Color figure can be viewed at wileyonlinelibrary.com.)

In terrestrial shocked zircons, the composition of entrained impact melt reflects partial melts of the original host (Moser et al. 2011) and possibly direct mineral melts (Davis 2017). We collected EDS element maps of zircon 14304 Z16 (Taylor et al. 2009), which contain multiple impact melt-filled veins, or curviplanar features decorated with impact melt inclusions that crosscut the zircon and are often associated with bright CL margins (Figs. 5A and 5B). Elemental maps in Figs. 5C–E show at least three distinct compositions of melt inclusions including (1) a K-Al-Si phase, (2) a Mg-Ca-Si phase, and (3) a Mg-Al phase. A similar K-Al-Si melt was described in veins in an alkali norite clast from 14304 by Goodrich et al. (1986), and the composition of phase (2) is also consistent with the pyroxene compositions within this clast. Phase (3) appears to contain Mg and Al with little to no Si suggesting that it may have a spinel-like composition; however, the elemental maps are not quantitative. The crosscutting nature and variable compositions of the melts further suggests an impact or multiple impact origin of the curviplanar features and melt inclusions.

Amorphous or Nanocrystalline Zircon

Only one zircon in the suite of grains analyzed contained regions of zircon composition that produced no discernible diffraction pattern. 15311 Z6 is highly shocked and contains numerous linear and curviplanar features entirely or partially filled with impact melt. Only the region that appears dark in the low kV BSE and bright in the CL images (Fig. 6) produces a discernible and indexable EBSP. This region also contains up to 28° of misorientation by CPD, one of the highest reported for lunar zircons to date (Grange et al. 2013a, 2013b). The majority of the zircon produces no diffraction pattern. There is no evidence of surface defects in the SE or BSE images, which suggests that the lack of a diffraction pattern is not a result of poor polishing. This implies that this region is either amorphous or nanocrystalline at length scales below the detection limit of EBSD analyses (~100 nm). Additional Raman spectroscopy analyses would be useful in determining if the zircon is nanocrystalline. For now, it is seen as amorphous, lacking long-range order at length scales >50 nm, a condition that can be due to metamictization (Nemchin et al. 2009a, 2009b) or shock metamorphism (Moser et al. 2011; Darling et al. 2016).

Planar and Spherical Shock Microtwins

We identified shock microtwins in four lunar zircons, all of which were separated from breccia samples (Table 1). EBSD analyses were used to

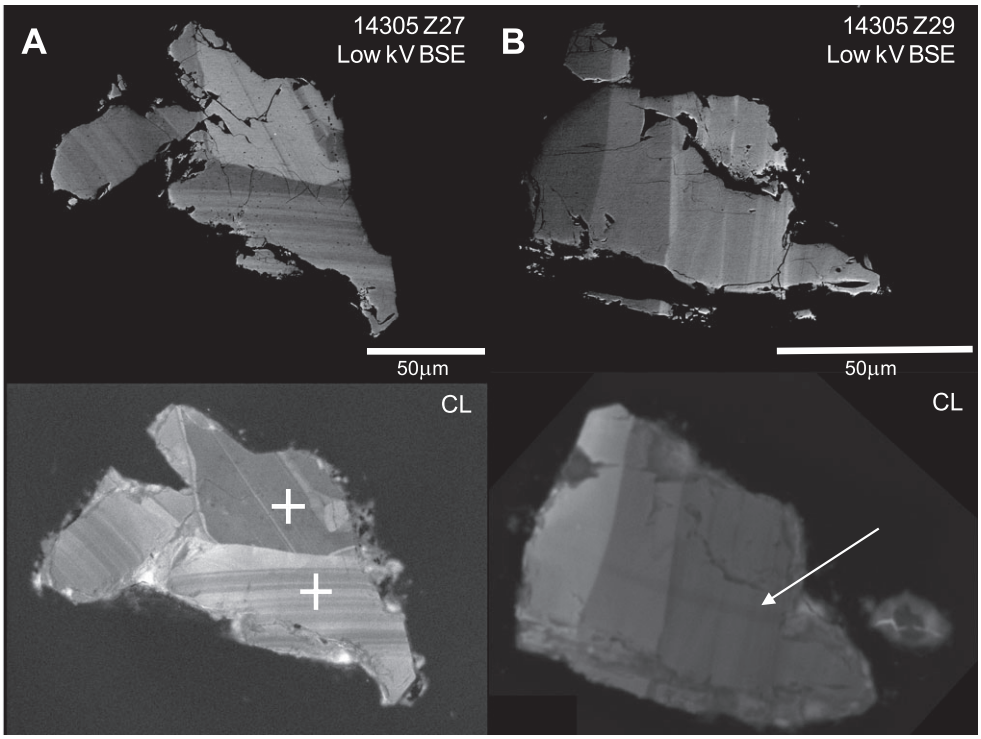

Fig. 2. Zircons exhibiting primary igneous zoning. A) Low kV BSE and CL images of 14305 Z27 (^{207}Pb-^{206}Pb age 4335 ± 13 Ma) showing well-preserved oscillatory zoning. The dark region is suggestive of a high-U core. EBSP analyses (+ symbols) show no variation in orientation between high- and low-U domains. Although the truncations of planar zoning in the dark domain by the lighter Cl region permits a multistage growth history, there is no variation in ^{207}Pb-^{206}Pb age with CL zonation in either of the grains shown here (Crow et al. 2017a). B) Low kV BSE and CL images of 14305 Z29 (^{207}Pb-^{206}Pb age 4254 ± 6 Ma; Table 1) showing primary sector zoning. EBSD line scan (dark band in CL image; denoted by arrow) also found no variation in orientation between domains; however, there is a slight decrease in band contrast in bright CL emission domains.

determine twin modes and crystallographic orientation. Two types of microtwins were identified. The first occurs in planar lamellae in which zircon exhibits an apparent 65° rotation around <010> relative to the host zircon lattice (Fig. 4). Planar twins are exemplified by breccia zircon 14305 Z36, which contains two bands that are comprised of three individual, parallel, twins each <1 μm in width (Fig. 4). The twins sharply terminate near the center where there is a high concentration of cracks, curviplanar features, and impact melt inclusions (right side of Fig. 4B). Similar termination, offset, or degradation of twins by curviplanar features has been observed in zircons from the Vrederfort impact structure (Moser et al. 2011). On the right edge of the grain, the twins are visible, but not as well defined and are parallel to two planar features with impact melt inclusions. The less defined twins also overlap a region of CPD that accommodates up to ~4° of misorientation about <001> (vertical bands in Fig. 4).

The second type of microtwinning occurs in ~5 μm wide lamellar domains that have curved borders with low degrees of curvature. They were first observed using low kV backscatter (channeling contrast) imaging that is not prone to geometric distortions that can be caused by charging and beam drift in EBSD analyses. The mircotwins are, therefore, short arcs to large radius circles (Fig. 7). If projected into a third dimension, the curved domains would map out as spherical shells containing zircon in twin orientation relative to the host. Within the shells, EBSD indicates that the twin mode is the same as that observed in the more common planar microtwin lamellae, i.e., the apparent rotation of twinning is <110>. Breccia zircon 14305 Z34 contains both types of shock microtwins, planar and spherical, as well as at least three other generations of shock microstructures (Fig. 7). Crosscutting relationships allow the microstructures to be placed in chronologic sequence. The oldest features are ~5 μm wide bands of primary oscillatory zoning that appear dark in CL and are associated with a reduction in EBSD indexing consistent with elevated U concentration from the time of crystallization on the Moon (Fig. 7B, D#1). The first shock-related feature is a set of three spherical shell microtwin domains that are up to ~10 μm wide (orange

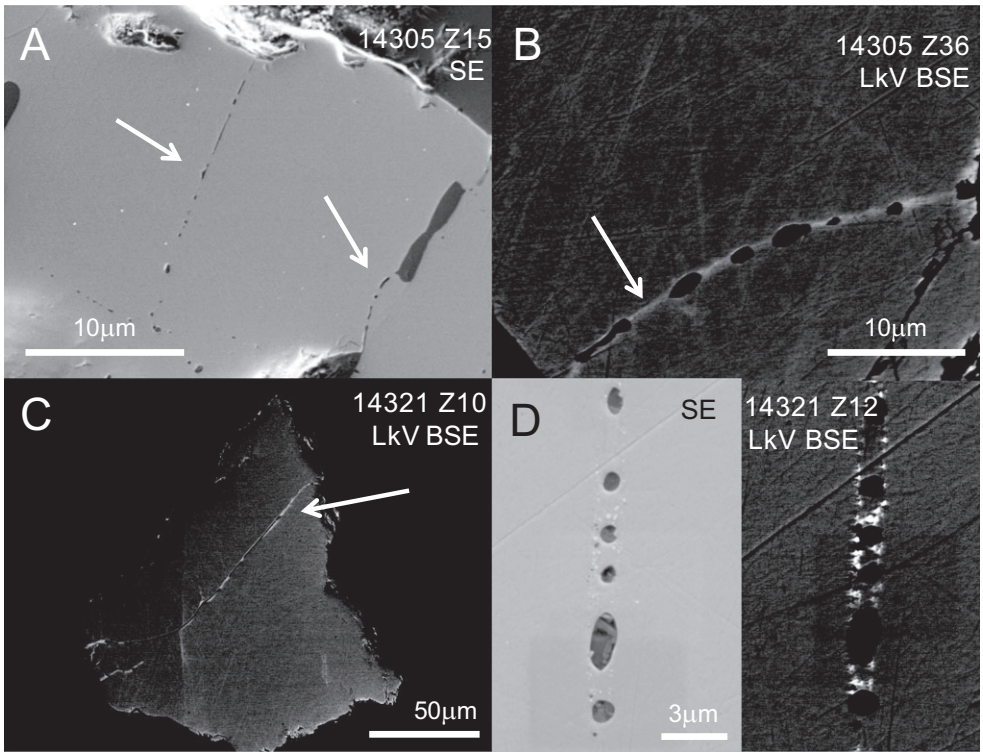

Fig. 3. Four examples showing the textures of secondary melt inclusions in zircon. A) Zircon 14305 Z15 contained the smallest impact melt glass inclusions observed, which are arranged mostly in linear arrays (white arrows). B) Bright low kV BSE regions (white arrow) associated with intermediate sized impact melt glass inclusions are suggestive of annealed curviplanar features and/or variations in trace element concentration (14305 Z36). These regions appear dark in CL images. C) Zircon 14321 Z10 represents the other endmember in which long segments of impact melt fill a fracture. The largest impact melt inclusions are often associated with variations in low kV BSE and CL (white arrow). D) A chain of ovoid inclusions along a lone linear feature in 14321 Z12 contains euhedral grains suggesting devitrification of the melt inclusions. Bright and dark spherical features surrounding inclusions are too small to be indexed by EBSD, but may be regions where the zircon has decomposed to its constituent oxides. (See Table 1 for ^{207}Pb-^{206}Pb ages.)

arcs in Fig. 7D#2) and are associated with chains of melt inclusions visible in the SE image (Fig. 7A). This is the first observation of spherical shell twins, to our knowledge. Like the linear twins in 14305 Z36, one of the spherical twins is discontinuous in a region with elevated impact melt inclusions in the center of the zircon. There is also a discontinuous zone containing zircon that is misoriented by up to 6° about the <001> of the primary zircon (Fig. 7D#3). There is no overlap of the discontinuous zone and the spherical twins, so it is not possible to determine if they are contemporaneous or sequential. A second planar shock microtwin offsets both the spherical twins and the discontinuous zone (pink twin in Fig. 7D#4). Stereographic projection maps show that each set of twins share one (110) plane with the primary zircon; however, the rotation axis of one twin is not parallel to the axis of the other. The latest structure in this sequence is a curviplanar annealed fracture zone running the length of the grain that accommodates up to 8° of lattice misorientation and offsets the primary zoning, spherical twins, and the discontinuous zone (Fig. 7D#5).

Granular Recrystallization

Postshock recrystallization was only observed in one of the lunar zircons in this microstructural survey in the form of granular texture recrystallization. The recrystallized region of 14305 Z30 is at an interface with pyroxene and consists of many ~1 μm to submicron zircon granules that are intergrown with pyroxene and exhibit random orientation relative to the host zircon (Figs. 8A–C). Zircon 14305 Z30 is pervasively crosscut by curviplanar annealed fractures hosting impact melt inclusions and exhibiting bright CL emitting margins. The CL pattern of the host grain shows a mottled texture, but no primary igneous zonation. Out of the 214 zircons analyzed at UCLA to date, only five zircons exhibit this thermal recrystallization texture (Crow et al. 2017a) suggesting that granular texture is rare in lunar zircons.

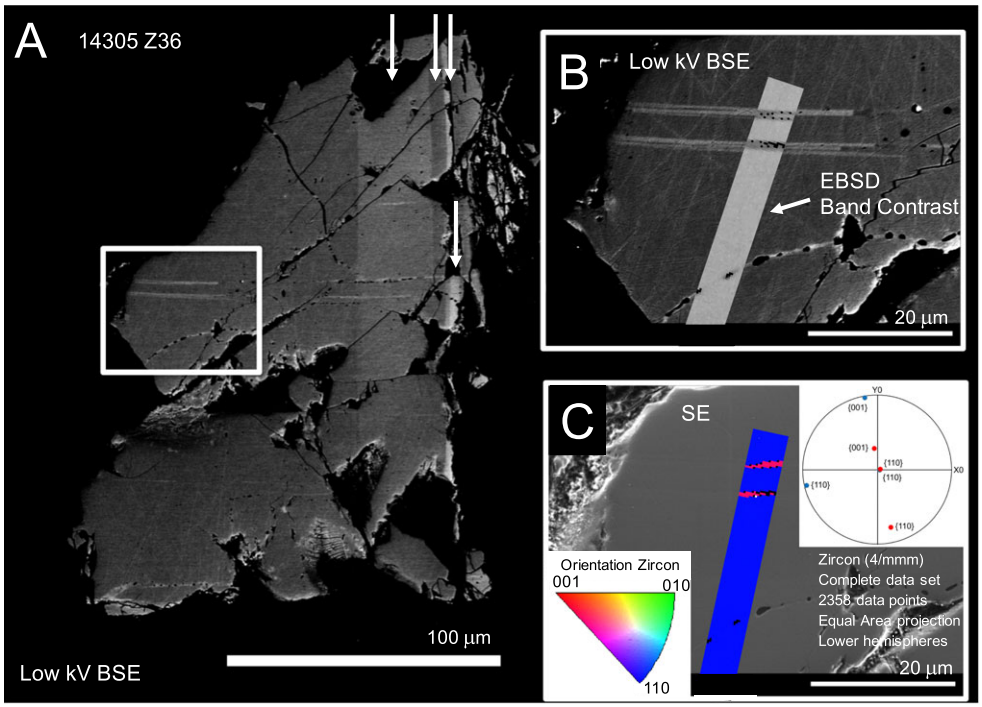

Fig. 4. A large zircon fragment from breccia 14305 (Z36, ^{207}Pb-^{206}Pb age of 4281 ± 5 Ma; Table 1) showing three stages of shock deformation. A) Low kV BSE image showing lamellae of twinned zircon that are crosscut by vertical, light and dark deformation bands (white arrows) that accommodate lattice crystal deformation about the c-axis of up to ~4°. The higher magnification images of the region defined by white box in BSE (B) and SE (C) show that the linear features are triplets. EBSD mapping reveals these features are microtwin lamellae with apparent rotation of 65° around <010> relative to the host zircon, which is illustrated by the EBSD overlay on the SE image. The c-axis is in the plane of the section with a north–south azimuth and the section is approximately parallel to {110}. Crosscutting deformation bands and microtwins are curviplanar features decorated or partly filled with secondary material (melt). (Color figure can be viewed at wileyonlinelibrary.com.)

Crystal-Plastic Deformation

Crystal-plastic deformation, i.e., pervasive, distributed lattice strain, was identified in eight (~20%; Table 1) of the lunar zircons. Four zircons contain bands of low angles of misorientation parallel to the c-axis. This type of deformation is most pronounced in breccia zircon 14305 Z25. The EBSD map in Fig. 9 reveals bands in {1K0} between ~3 and 10 µm in width that accommodate up to ~5° by slip in the {001} plane. The boundaries between the bands appear as slight depressions in SE images due to preferential polishing, and in some places the boundaries host impact melt inclusions. This grain also has primary igneous zoning seen in the CL image (Fig. 9C), which is crosscut by the banded deformation. Four of the lunar zircons exhibit CPD that is not related to lattice rotation about the c-axis, and most of this deformation appears to be associated with zones of annealed fractures (e.g., breccia zircon 14305 Z34; Fig. 7D#5). In all cases of CPD in this subset of samples, the misorientation does not exceed ~8° relative to the host grain, except for zircon 15311 Z6 discussed previously.

DISCUSSION

The primary objective of our microstructural analyses was to document the range of microstructures in lunar zircons in an attempt to reconstruct the impact conditions experienced by these samples. A secondary objective was to produce a catalog of high-resolution SEM images of impact shock features that could be useful for identifying similar microstructures in other lunar zircon samples (see supporting information). Similar compilations of shock microstructures for terrestrial zircons have been reported for samples of deep crust from a large central uplift (Moser et al. 2011) as well as the upper level and ejecta facies of craters (Timms et al. 2017). The lunar zircons we analyzed exhibit nearly the complete range of shock microstructures previously observed in terrestrial impact zircons, except for formation of the high-pressure polymorph reidite. In the case of breccia 14305, the full suite of microstructures described, including a previously unidentified morphology of shock microtwins, are observed in zircons separated from a single 16 g rock fragment. Although the survey size of

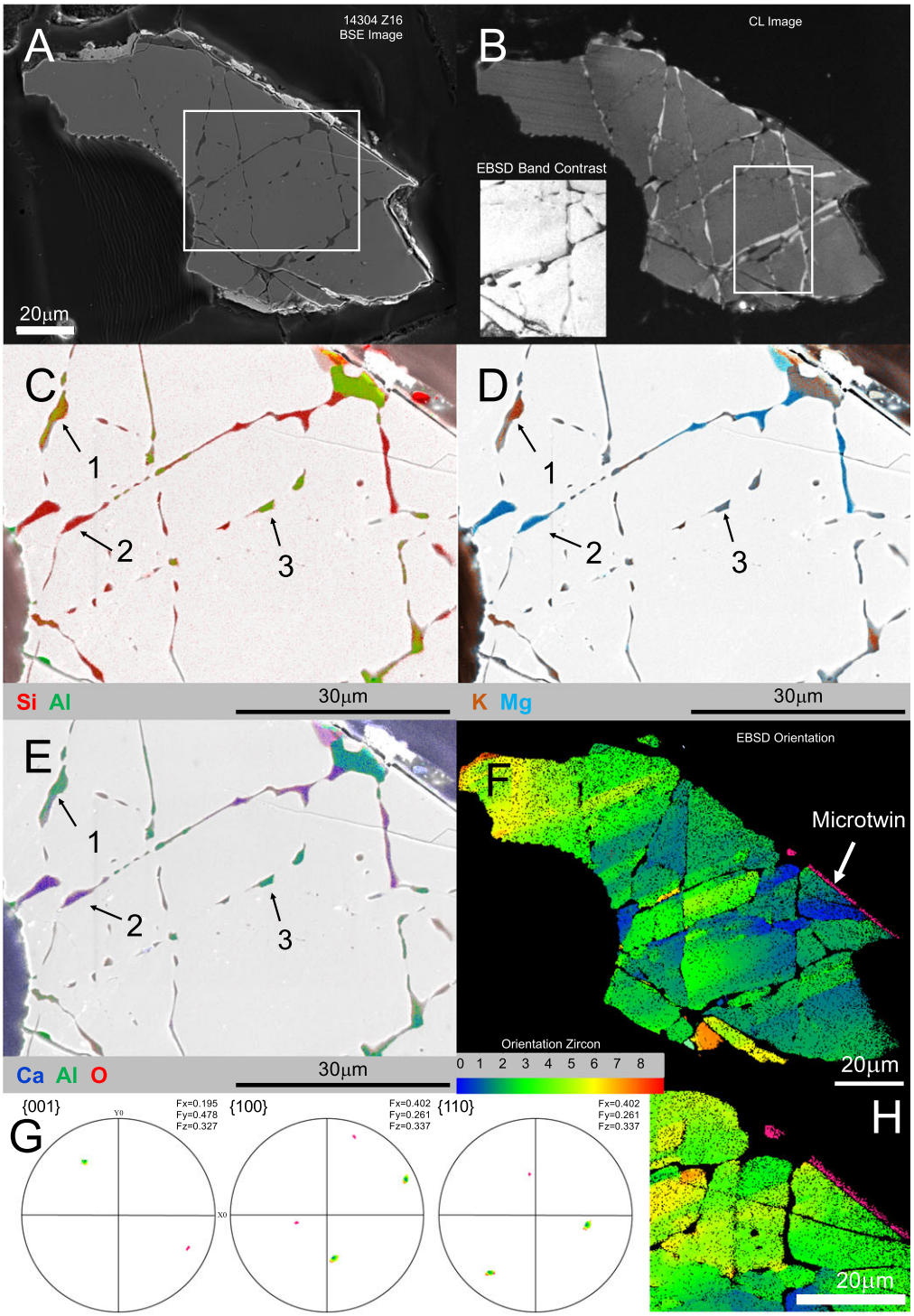

Fig. 5. SE (A) and CL (B) images of 14304 Z16 (^{207}Pb-^{206}Pb age of 4246 ± 26 Ma; Table 1) reveals a conjugate network of subplanar features, likely shock microstructures, either partially or totally filled with melt or decorated with micron-scale inclusions. EDS analyses (C–E) reveal three compositions of glass (1) a K-Al-Si phase, (2) a Mg-Ca-Si phase, and (3) a Mg-Al phase. Veins of K-Al-Si glass were reported in an alkali norite clast from 14304 suggesting that these two samples may be related. EBSD analyses (F) reveal up to ~7° of misorientation within the host zircon as well as a shock microtwin (pink twin in F and H). The twin and host zircon share one {110} axis (G). Note that the melt-filled features appear to crosscut the microtwin indicating that melt injection postdated twinning. (Color figure can be viewed at wileyonlinelibrary.com.)

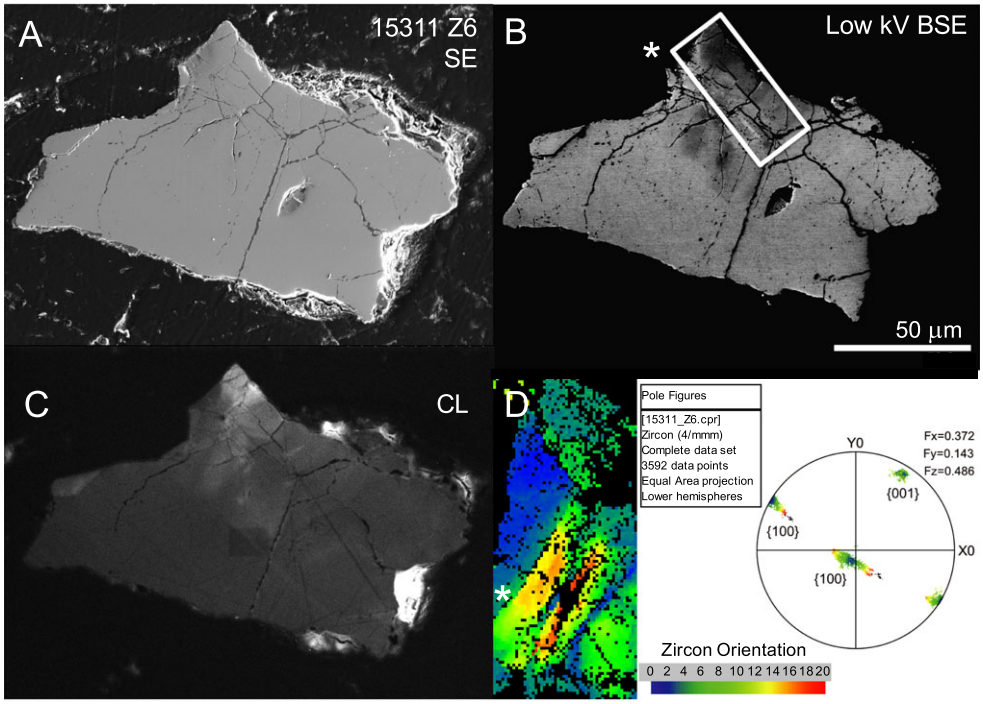

Fig. 6. SE (A) and BSE (B) images of a lunar soil zircon 15311 Z6. This ~4.30 Ga (Table 1) grain contains an intricate network of linear and curviplanar features either partially or totally filled with impact melt (Crow et al. 2017a). C) Zircon domains that are dark in CL yield no or very weak electron diffraction suggesting that these regions are essentially amorphous (disordered at the ~100 nm spatial resolution of the analysis) or are nanocrystalline below the resolution of the EBSD analyses. D) An EBSD map for the regions that did produce reliably indexed patterns (white box B) reveals up to 28° of misorientation accommodated across linear and curviplanar features. The calculated α-dose for this grain is high enough to cause partial metamictization. (Color figure can be viewed at wileyonlinelibrary.com.)

31 zircons may not be sufficiently large to be statistically robust, paired with previously reported microstructural analyses, there are still generalizations that can be made about the lunar zircon shock microstructures that enable us to place constraints on shock pressure and temperature histories.

Spherical Twins: A New Shock Microstructure Morphology

Spherical twins have not been previously reported in either terrestrial or lunar zircons, so further discussion of their morphology and formation is warranted. One possible explanation for the ~15° curvature is CPD of an originally planar twin. If the twins' domain is perpendicular to the surface, the host zircon would need to share the ~15° of deformation. However, <1° of misorientation is observed across the host zircon save for the annealed fracture and discontinuous zone discussed above. Additionally, linear primary igneous zonation does not seem to be affected by either the curved or linear microtwins (Fig. 7B). It is, therefore, unlikely that deformation of planar twins is the formation mechanism for the spherical twins. Instead, we favor a nucleation model that involves modification of pre-existing defects. All three spherical twins are spatially aligned with chains of impact melt inclusions, allowing that altered physical properties of the crystal associated with melt injection along curved fracture networks could promote different twinning behavior. Certainly the morphometry of these features is more akin to fracturing resulting from shock induced tensile stress (i.e., spallation fracturing) seen in laser driven ballistic experiments (e.g., Bolis et al. 2007; Cuq-Lelandais et al. 2009). This type of modification has not been observed in terrestrial samples; however, the lunar zircons are unique in that they have been subjected to multiple impact events. To date, no experiments have been conducted to determine the effects of multiple shock events on zircon crystal structures, but the multiple types and crosscutting sequence of unaligned microdeformations in this grain make it a candidate for such a history.

Constraints on Pressure and Temperature

Shock Pressures and Strain Rates

Linear and curviplanar features hosting impact melt inclusions are the most common shock features in the lunar zircons, and they are present in grains that span

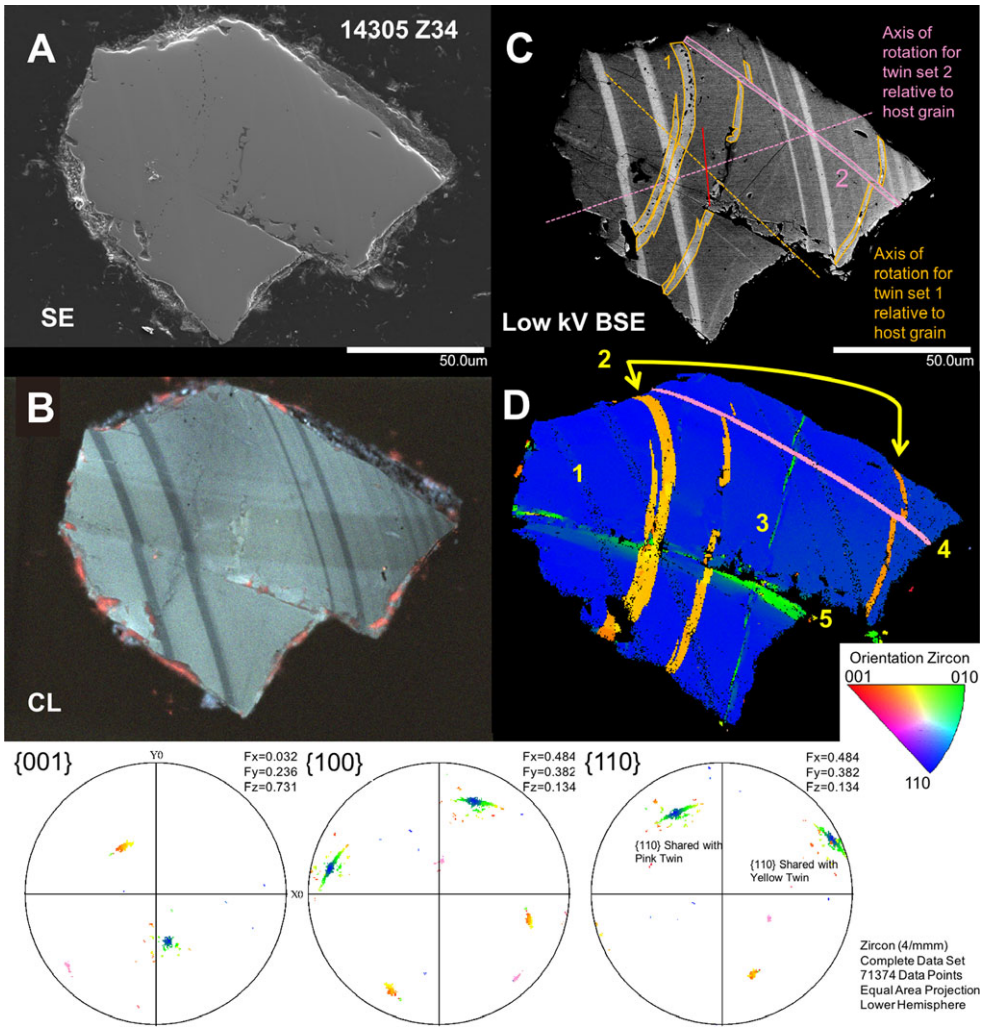

Fig. 7. SEM images of zircon 14305 Z34 (^{207}Pb-^{206}Pb age of 4324 ± 5 Ma; Table 1) illustrating arc-shaped shock microstructures (spherical, if projected in third dimension) that so far are unique to the Moon. SE image (A) reveals secondary melt inclusions outlining concentric, arc-shaped chains (left side). B) Apparent primary igneous zonation appears as dark bands in CL image and is associated with bright low kV BSE response (C). These bands also have reduced band contrast and a higher concentration of unindexed pixels in EBSD (D). Low kV BSE image (C) and EBSD map (D) show two sets offsetting microtwins, i.e., (1) arc-shaped or spherical twins (orange) and (2) linear twin (pink). Both sets of twins share a {110} axis with the host zircon (steronet plots); the axis of rotation of spherical twins (set 1) and planar twin (set 2) are shown in (C). EBSD crystal orientation map (D) showing a sequence of microstructural evolution from oldest to youngest based on crosscutting relationships; (1) primary igneous zonation, (2) spherical microtwins (65° rotation about [1¯10]), (3) planar deformation feature, (4) planar microtwin (65° rotation about [110]), (5) linear fracture accommodating up to 8° of deformation. (Color figure can be viewed at wileyonlinelibrary.com.)

almost the full range of zircon ^{207}Pb-^{206}Pb crystallization ages from ~4.0 to 4.4 Ma (Crow et al. 2017a). The morphologies of these inclusions are similar in the Vredefort and lunar zircons suggesting formation by a similar mechanism, i.e., injection of partial melt of surrounding phases into fractures during rarefaction or shock unloading (Moser et al. 2011). Davis (2017) suggested that the Vredefort zircon melt inclusions formed at shock pressures as low as 3–5 GPa based on the identification of coesite in outcrops along strike from the zircon source rocks. Linear features have also been observed in zircons experimentally shocked to pressures above 20 GPa and are attributed to high densities of defects along glide planes; however, neither curviplanar features nor impact melt inclusions were noted (Leroux et al. 1999). There are multiple parameters that vary between experimental and natural samples, such as target host materials and grain orientation, which could be a source of the observational variations. It was difficult to assess the

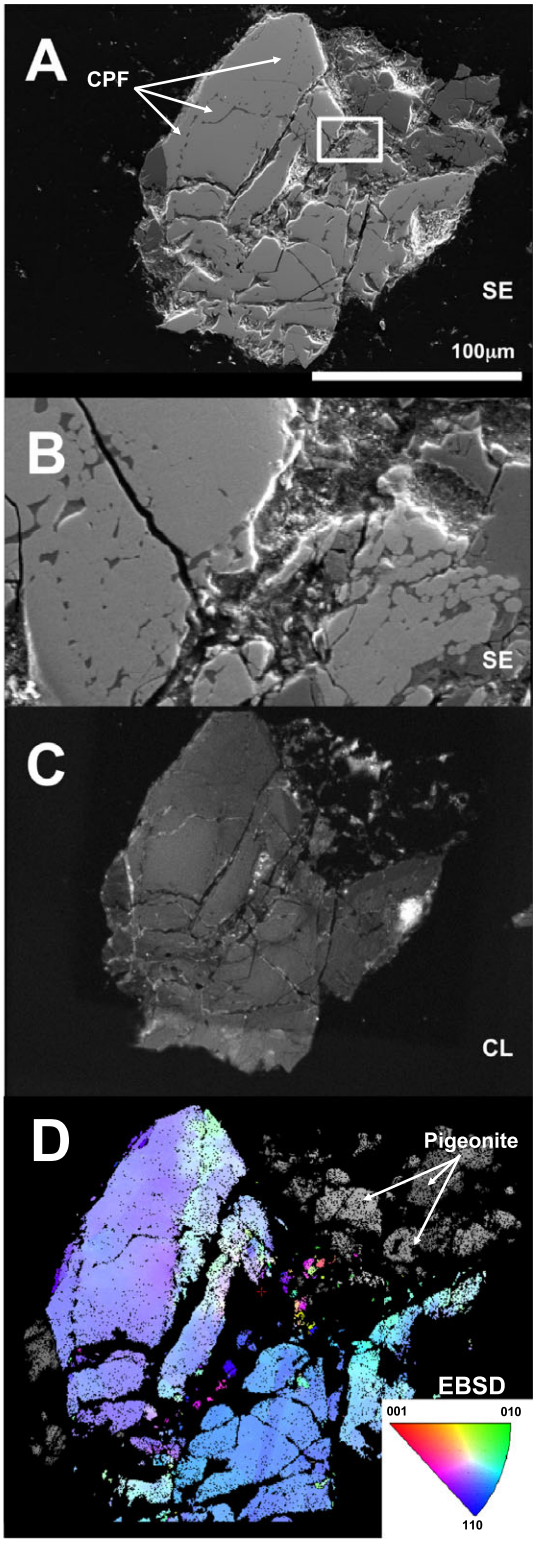

Fig. 8. SEM images and EBSD map of highly shocked zircon 14305 Z30, which exhibits local recrystallization and granular texture in contact with igneous minerals. The SE image (A) reveals a zircon in contact with pigeonite with a network of melt-filled curviplanar features (CPF) crosscut by more recent, open fractures. The higher resolution image (B) of the central region (~17 μm white box in A) reveals patches of micron-scale, coarse granular texture and zircon neoblasts. The CL image in (C) shows a complicated mixture of textures including annealed and melt-filled curviplanar features with bright CL margins, mottled regions, and possible relict primary zoning. The EBSD orientation map (D) of the zircon highlights the finer scale orientation variations in the granular texture region. Pigeonite was indexed and appears gray in EBSD map (orientation not shown). (Color figure can be viewed at wileyonlinelibrary.com.)

occurrence of curviplanar features in previously published lunar zircon analyses due to low resolution images; however, planar features were described or visible in ~35% of grains (see supporting information). The prevalence of both linear and curviplanar features is not surprising since their formation requires the lowest levels of shock pressure (Timms et al. 2012), and suggests that the majority of lunar zircons have been exposed to shock pressures of at least ~3–20 GPa (Leroux et al. 1999; Moser et al. 2011; Davis 2017).

At higher shock pressures, zircon can convert to the high-pressure polymorph, reidite. It has been experimentally demonstrated that shocked zircons start to develop reidite domains at pressures >40 GPa in dehydrated conditions (Leroux et al. 1999). Shock microtwins with reidite twin orientation, but zircon crystal structure, have also been observed in zircons from terrestrial impact ejecta deposits and thought to reflect reversion of reidite back to zircon (e.g., Timms et al. 2017). No lunar zircon analyzed by EBSD to date retains evidence of reidite or reidite reversion suggesting that these grains have not experienced shock pressures >40 GPa.

Shock microtwins were identified in only ~10% of the lunar zircons in this study. Microtwins have been considered indicative of some of the highest shock pressures; however, recent work by Morozova et al. (2017) has produced microtwins at static pressures below ~11 GPa when high strain rates were applied by means of a diamond anvil cell under dehydrated conditions. In these experiments, the pressure was incrementally increased in steps of 1 GPa with 15 min between each step, and the total time to manually increase the pressure by 1 GPa was on the order of seconds. The relative scarcity of lunar zircons containing microtwins suggests that only a small fraction have been subject to high strain rates necessary for microtwin formation. Moreover, the dearth of these features cannot be explained by destruction during subsequent impact events. This follows from the observation of multiple, offsetting shock twins within zircon 14305 Z34 and the preservation of twin

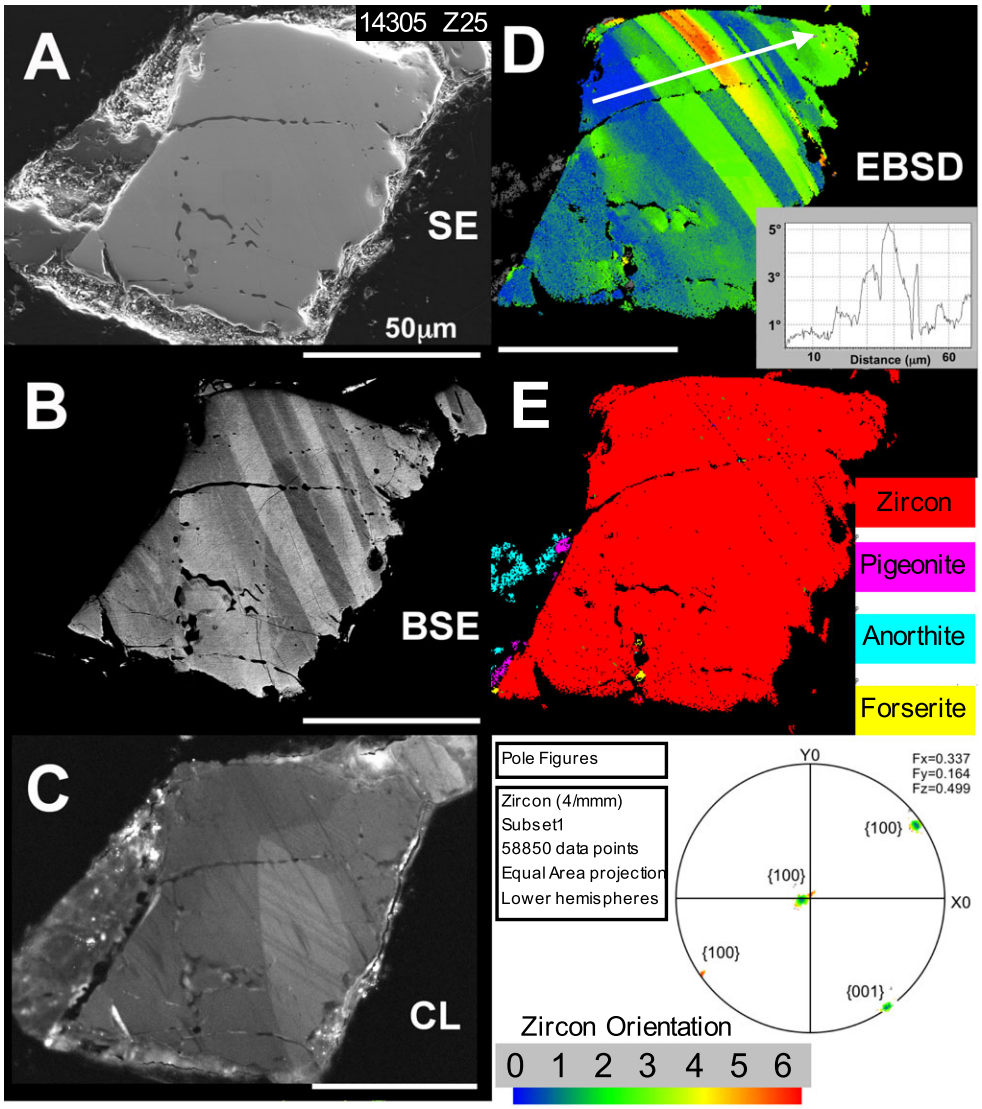

Fig. 9. Images of zircon 14305 Z25 illustrating deformation bands in {1K0} accommodating several degrees of lattice orientation and crystal-plastic deformation in the {001} plane (^{207}Pb-^{206}Pb age of 4265 ± 5 Ma; Table 1). A) SE image revealing curviplanar features filled to partly decorated with impact melt, as well as contact with plagioclase, pigeonite, and minor olivine (E). B) Low kV BSE image shows evidence for lattice orientation change and primary zonation. C) CL image exhibiting primary sector and oscillatory zoning. The CL zoning is associated with weak variations in the BSE image (B). D) EBSD orientation map and profile (white arrow) showing up to 5° misorientation across c-axis parallel bands. Pole figure and orientation key are in bottom right of figure. (Color figure can be viewed at wileyonlinelibrary.com.)

orientation in terrestrial samples during impact-related heating and reidite reversion (Moser et al. 2011; Timms et al. 2017).

Maximum Temperatures

High-temperature recrystallization or decomposition to ZrO_2 and SiO_2 are rare in lunar zircons. In our survey, recrystallization was observed only in 14305 Z30. The recrystallized granules in this grain are similar to the dissociated neoblasts in zircons found in ejecta glasses from the Acraman impact structure presented in Timms et al. (2017) in that they are small and are randomly oriented relative to the host grain (Fig. 8B). 14305 Z30 differs in that it does not contain evidence of decomposition to ZrO_2 and SiO_2, formation of twins, or conversion to reidite. The absence of these structures suggests that this zircon did not experience temperatures above ~1690 °C or pressures within the stability field of reidite (Butterman and Foster 1967). However, the presence of the granules suggests temperatures of at least ~900–1000 °C, which is necessary to recrystallize damaged zircon (Weber 1990; Weber et al. 1994;

Reimold and Gibson 1996; Gibson et al. 1997). Recrystallization textures have previously been observed in four zircons from Apollo 15 and 17 samples (Nemchin et al. 2008; Grange et al. 2009, 2013a, 2013b; Crow et al. 2017a, 2017b) and decomposition has been confirmed in four Apollo 15 zircons (Grange et al. 2013b; Bellucci et al. 2016; Crow et al. 2017a, 2017b) (see supporting information). Two of the 14311 zircons from Hopkins and Mojzsis (2015) appear to have decomposition textures; however, no compositional or structural analyses were reported for these grains. A polycrystalline texture zircon with vesicles and associated baddeleyite was also identified in lunar meteorite Dhofar 458 (Zhang et al. 2011). In total, only ~2% of the zircons analyzed at UCLA to date and ~7% of previously reported zircons contain recrystallized domains or dissociation textures suggesting that >93% of the lunar zircons have not experienced post crystallization temperatures in excess of ~1000 °C.

This conclusion is also supported by the preservation of melt inclusions without obvious signs of recrystallization. Zircon 14321 Z12 is the only grain in this survey that contains crystalline impact melt inclusions, which suggests it was heated above the glass transition temperature of silicate glasses (~1000 °C) in a later thermal event that may have been impact related (Brückner 1970; Avramov et al. 2005; Cormier et al. 2005). Recrystallization of the melt inclusions, which are at most ~3 μm long, would only require high temperatures a short duration. von Engelhardt et al. (1995) conducted devitrification experiments on suevite glasses and observed pyroxene crystals in glass samples after only 1 h of annealing between ~800 and 1000 °C. This is the only observation of devitrified melt inclusions in the lunar zircons, to our knowledge.

Preservation of crystal lattice damage or nanocrystalline domains in 15311 Z6 is also indicative of low maximum temperatures. This grain has a U concentration of 114 ppm and Th concentration of 74 ppm, which are about twice the average concentrations in lunar zircons (~50 ppm and ~40 ppm, respectively; Crow et al. 2017a, 2017b). Using the oldest age for this sample from Crow et al. (2017a, 2017b) (^{207}Pb-^{206}Pb ages range from 4245 ± 4 to 4332 ± 3 [1σ] Ma) and the methods from Murakami et al. (1991), we calculate a total α-dose of 3.5×10^{15} α/mg, which agrees well with the values reported for Apollo 14 zircons of a similar U concentration by Pidgeon et al. (2016). This value is above the α-dose necessary for Stage I radiation damage and well within the domain of Stage II damage (>2.2×10^{15} α/mg); however, it is below the dose at which zircon becomes dominated by amorphous domains (>8×10^{15} α/mg) (Murakami et al. 1991; Zhang et al. 2000; Pidgeon 2014; Pidgeon et al. 2016). Previous authors have estimated that temperatures of ~230 °C are necessary to anneal Stage I damage and temperatures above 1000 °C are necessary to recrystallize amorphous zircon (Weber 1990; Weber et al. 1994; Pidgeon 2014). Preservation of α-damage in 15311 Z6 implies that it must not have been exposed to temperature above 1000 °C for significant time.

Implications for Petrogenesis

The majority of lunar zircons are detrital, and those with adjacent phases have shock microstructures that terminate at grain boundaries making it difficult to determine the parent rock composition. The fragmented nature of these samples and the preservation of offsetting impact shock microstructures suggest that some of these zircons experienced multiple impact events. This is not unexpected since the lunar surface has been heavily bombarded resulting in impact craters ranging in size from large impact basins to micrometeorite impact craters. The estimated number of >200 km diameter lunar basins determined by the NASA GRAIL Mission exceeds 70 (Neumann et al. 2015) and the number of basins >100 km is in excess of ~200 (Losiak et al. 2009; Head et al. 2010). Additionally, some lunar highlands regions have reached saturation for craters on the order of 20 km (Head et al. 2010). For comparison, the diameters of the Vrederfort impact basin, Sudbury impact basin, and Ries crater are ~300, 130, and 24 km, respectively (Pope et al. 2004; Gibson and Reimold 2008; Stöffler et al. 2013; supporting information). Zircons from all three sites contain evidence of impact modification, so it is expected that most lunar zircons should contain impact shock microstructures (e.g., El Goresy 1965; Krogh et al. 1984; Wittmann et al. 2006; Moser et al. 2011; Timms et al. 2017).

As discussed in the Overview of Shock Microstructures in Zircon section, the types of zircon shock microstructures observed differ between samples of impact ejecta and samples of crust beneath the crater floor. For microstructures like shock microtwins and the transition to reidite, it is widely accepted that these features can only form in an impact environment. However, other microstructures, such as recrystallization and CPD, can occur in both impact and tectonic environments. For example, both banded and unbanded CPD has been observed in tectonically deformed terrestrial zircons (e.g., Reddy et al. 2007). In cases of CPD observed in impact environments, like the Vrederfort structure, it is most likely a result of impact induced tectonism due to formation of the central uplift and subsequent settling of the crater floor (Moser et al. 2011). It is therefore difficult to determine the catalyst

responsible for the CPD. Similarly, granular texture crystallization, such as that in 14305 Z30, can be produced in zircon under amphibolite–granulite facies conditions in tectonic settings (e.g., Cavosie et al. 2015a). Lunar granulites have been identified in the Apollo collection; however, the high equilibration temperatures and elevated highly siderophile compositions of these rocks suggest that the heat source for metamorphism was impact derived (i.e., melt sheet, ejecta blanket) (e.g., Cushing et al. 1999; Hudgins et al. 2008; McLeod et al. 2016). Regardless, the occurrence of high temperature recrystallization in the lunar zircons is rare and ~30% of the samples exhibit CPD.

Models of complex lunar craters suggest that central uplifts and rims would accumulate the highest amounts of plastic strain, whereas the highest levels of shock pressure would be experienced by ejecta and the brecciated lens of material below the crater floor (e.g., Collins et al. 2002). The latter materials would also experience elevated temperatures for long durations, possibly sufficient to recrystallize or decompose zircon. These conditions are reflected in the observation of neoblastic recrystallization in the central region of Vredefort and decomposed zircon identified in ejecta materials from the Acraman impact structure in Australia (Moser et al. 2011; Timms et al. 2017). The microstructures of the lunar zircons are, therefore, most consistent with the conditions expected in the rim(s) of complex craters and basins, where strain rates are high, but peak temperatures and shock pressures would be moderate to low.

This conclusion is consistent with the sampling location of the Apollo 15 mission, which is situated on the rim of the Imbrium basin (see map in supporting information). The Apollo 14 landing site is located in the Fra Mauro formation, which is thought to be a combination of locally derived material and ejecta from the Imbrium basin-forming event (Wilshire and Jackson 1972; Swann et al. 1977). The absence of reidite and little evidence of textures common in ejecta grains may suggest that this set of Apollo 14 zircons do not represent Imbrium ejecta, but rather material derived from more local cratering events. The landing site is ~30 km north of the rim of Fra Mauro crater, which is a complex crater with a diameter of ~95 km (Swann et al. 1977), and <200 km north of the rim of Nubium basin (~690 km; Wilhelms 1987; Neumann et al. 2015). Some of the Apollo 14 zircons do show evidence of high-temperature alteration (>1000 °C) suggesting original emplacement within the central uplift or near the crater floor (Table 1 and supporting information). However, these samples are rare and could be explained by transport due to excavation by subsequent cratering events. For example, there is evidence of similar transport of material to the Apollo landing sites via the Copernicus impact event from ^{40}Ar-^{39}Ar analyses and thermal modeling of an Apollo 12 impact melt breccia 12033 (Crow et al. 2017b). The scarcity of the high-temperature recrystallization and decomposition textures, which are often associated with Pb-loss in zircon, may also explain why the ages of the Imbrium and Serenitatis impacts are not well represented in the lunar zircon U-Pb systematics (Meyer et al. 1996; Nemchin et al. 2006, 2008; Pidgeon et al. 2007; Taylor et al. 2009; Grange et al. 2013a, 2013b; Hopkins and Mojzsis 2015; Crow et al. 2017a).

CONCLUSION AND SUMMARY

Our microstructural survey of Apollo 14 and 15 zircons reveals that a large fraction of the lunar grains have experienced minimum shock pressures between 3 and 20 GPa, few contain evidence of temperatures above 1000 °C, and no samples record shock pressures in excess of 40 GPa. This range of pressures and temperatures are typically observed in the uplifted materials in rims of large impact craters and materials within the crater subsurface. Only a few lunar zircons contain fine grained recrystallization or dissociation to ZrO_2 and SiO_2 and may represent samples of the higher temperature regions in the central uplift or possibly ejecta deposits; however, these grains are uncommon in the Apollo collection. The zircon high-pressure polymorph reidite has yet to be observed in lunar samples, which also suggests these samples have not experienced high shock pressures (>40 GPa) that are characteristic of impact ejecta. This may imply that the Apollo zircons reported herein represent locally derived materials and not ejecta from Imbrium or the other nearside basins.

In addition to constraining the impact shock pressure and temperature conditions recorded in the lunar zircons, we have also identified a novel morphology of shock microtwins that is best described as spherical shells of twinning zircon. The association of the spherical shell microtwins with curviplanar chains of impact melt glass inclusions and the lack of CPD of the host grain suggests this type of twin may nucleate on pre-existing curviplanar features. Paired with the observations of offsetting relationships between microstructures, this suggests that some lunar zircons record evidence of multiple impact shock events. Experiments into the effects of multiple shock events on the zircons microstructures would be useful in future interpretation of the lunar zircon textures.

Acknowledgments—The authors thank NASA CAPTEM for allocating the Apollo samples for this study, Dianne

Taylor for her assistance with zircon separations and initial imaging, and Ivan Barker at the Zircon and Accessory Phase Laboratory for his work collecting EBSD analyses. We also thank James Darling, Joshua Snape, and Katie Joy for their constructive and insightful reviews. We also acknowledge and thank Axel Wittman, Marion Grange, and an anonymous reviewer for their input on a previous version of this manuscript. This work was supported in part by the NASA Earth and Space Sciences Fellowship and the NASA Cosmochemistry and NSF Instrumentation and Facility programs, as well as by an NSERC Discovery Grant to Desmond Moser. This manuscript was prepared in part at Lawrence Livermore National Laboratory under Contract DE-AC52-07NA27344.

Editorial Handling—Dr. Katherine Joy

REFERENCES

Avramov I., Vassilev T., and Penkov I. 2005. The glass transition temperature of silicate and borate glasses. *Journal of Non-Crystalline Solids* 351:472–476.

Barboni M., Boehnke P., Keller B., Kohl I. E., Schoene B., Young E. D., and McKeegan K. D. 2017. Early formation of the Moon 4.51 billion years ago. *Science Advances* 3:1.

Bellucci J. J., Whitehouse M. J., Nemchin A. A., Snape J. F., Pidgeon R. T., Grange M., Reddy S. M., and Timms N. 2016. A scanning ion imaging investigation into the mircron-scale U–Pb systematics in a complex lunar zircon. *Chemical Geology* 438:112–122.

Blanc P., Baumer A., Cesborn F., Ohnenstetter D., Panczer G., and Rémond G. 2000. Systematic cathodoluminescence spectral analysis of synthetic doped minerals: Anhydrite, apatite, calcite, fluorite, scheelite and zircon. In *Cathodoluminescence in geosciences*, edited by Pagel M., Barbin V., Blanc P., and Ohnenstetter D. Berlin: Springer. pp. 127–160.

Bohor B. F., Betterton W. J., and Krogh T. E. 1993. Impact-shocked zircons: Discovery of shock-induced textures reflecting increasing degrees of shock metamorphism. *Earth and Planetary Science Letters* 119:419–424.

Bolis C., Berthe L., Boustie M., Arrigoni M., Barradas S., and Jeandin M. 2007. Physical approach to adhesion testing using laser-driven shock waves. *Journal of Physics D: Applied Physics* 40:3155–3163.

Brückner R. 1970. Properties and structure of vitreous silica. I. *Journal of Non-Crystalline Solids* 5:123–175.

Butterman W. C. and Foster W. R. 1967. Zircon stability and the ZrO_2-SiO_2 phase diagram. *American Mineralogist* 52:880–885.

Cavosie A. J., Erickson T. M., and Timms N. E. 2015a. Nanoscale records of ancient shock deformation: Reidite ($ZrSiO_4$) in sandstone at the Ordovician Rock Elm impact crater. *Geology* 43:315–318.

Cavosie A. J., Erickson T. M., Timms N. E., Reddy S. M., Talavera C., Montalvo S. D., Pincus M. R., Gibbon R. J., and Moser D. E. 2015b. A terrestrial persepective on using ex situ shocked zircons to date lunar impacts. *Geology* 43:999–1002.

Cavosie A. J., Timms N. E., Erickson T. M., Hagerty J. J., and Hörz F. 2016. Transformations to granular zircon revealed: Twinning, reidite, and ZrO2 in shocked zircon from Meteor Crater (Arizona, USA). *Geology* 44:703–706.

Church S. E., Tilton G. R., and Chen J. H. 1976. Lead isotopic studies of lunar soils: Their bearing on the time scale of agglutinate formation. Proceedings, 7th Lunar Science Conference. pp. 351–371.

Collins G. S., Melosh H. J., Morgan J. V., and Warner M. R. 2002. Hydrocode simulations of Chicxulub crater collapse and peak-ring formation. *Icarus* 157:24–33.

Corfu F., Hanchar J. M., Hoskin P. W. O., and Kinney P. 2003. Atlas of zircon textures. *Reviews in Mineralogy and Geochemistry* 53:468–500.

Cormier L., Neuville D. R., and Calas G. 2005. Relationship between structure and glass transition temperature in low-silica calcium aluminosolicate glasses: The origin of the anomaly at low silica content. *Journal of the American Ceramic Society* 88:2292–2299.

Crow C. A., McKeegan K. D., and Moser D. E. 2017a. Coordinated U-Pb geochronology, trace elements, Ti-in-zircon thermometry and microstructural analysis of Apollo zircons. *Geochimica et Cosmochimica Acta* 202:264–284.

Crow C. A., Cassata W. S., Jolliff B. L., Zeigler R. A., Borg L. E., and Shearer C. K. 2017b. Ar-Ar thermochronology of Apollo 12 impact-melt breccia 12033,638-1 (abstract #2823). 22nd Lunar and Planetary Science Conference. CD-ROM.

Cuq-Lelandais J. P., Boustie M., Berthe L., De Rességuier T., Combis P., Colombier J. P., Nivard M., and Claverie A. 2009. Spallation generated by femtosecond laser driven shocks in thin metallic targets. *Journal of Physics D: Applied Physics* 42:065402.

Cushing J. A., Taylor G. J., Norman M. D., and Keil K. 1999. The granulitic impactite suite: Impact melts and metamorphic breccias of the early lunar crust. *Meteoritics & Planetary Science* 34:185–195.

Dalrymple G. B. and Ryder G. 1996. Argon-40/argon-39 age spectra of Apollo 17 highlands breccia samples by laser step heating and the age of the Serenitatis basin. *Journal of Geophysical Research* 101:26,069–26,084.

Darling J. R., Moser D. E., Barker I. R., Tait K. T., Chamberlain K. R., Schmitt A. K., and Hyde B. C. 2016. Variable microstructural response of baddeleyite to shock metamorphism in young basaltic shergottite NWA 5298 and improved U-Pb dating of solar system events. *Earth and Planetary Science Letters* 444:1–12.

Davis C. L. 2017. Microstructural geochronology of zircon across the central uplift of the Vrederfort impact structure, South Africa. M.Sc. thesis, Western University, London, Ontario, Canada.

El Goresy A. 1965. Baddeleyite and its significance in impact glasses. *Journal of Geophysical Research* 70:3453–3456.

Engelhardt W. von, Arndt J., Fecker B., and Pankau H. G. 1995. Suevite breccia from the Ries crater, Germany: Origin, cooling history and devitrification of impact glasses. *Meteoritics* 30:279–293.

Engelhardt W. von, Ardnt J., Stöffler D., and Schneider H. 1972. Apollo 14 regolith and fragmental rocks, their compositions and origin by impacts. Proceedings, 3rd Lunar Science Conference. pp. 753–770.

Erickson T. M., Cavosie A. J., Moser D. E., Barker I. R., and Radovan H. A. 2013a. Correlating planar microstructures in shocked zircon from the Vredefort Dome at multiple

scales: Crystallographic modeling, external and internal imaging, and EBSD structural analysis. *American Mineralogist* 98:53–65.

Erickson T. M., Cavosie A. J., Moser D. E., Barker I. R., Radovan H. A., and Wooden J. 2013b. Identification and provenance determination of distally transported, Vrederfort-shocked minerals in the Vaal River, South Africa using SEM and SHRIMP-RG techniques. *Geochimica et Cosmochimica Acta* 107:170–188.

French B. M. 1968. Shock metamorphism as a geological process. In *Shock metamorphism of natural materials*, edited by French B. M. and Short N. M. Baltimore, Maryland: Mono Book Corp. pp. 1–17.

Gibson R. L. and Reimold W. U. 2008. Geology of the Vredefort impact structure, a guide to sites of interest. *Memoir, Council of Geoscience, Pretoria* 97:181.

Gibson R. L., Armstrong R. A., and Reimold W. U. 1997. The age and thermal evolution of the Vredefort impact structure: A single-grain U-Pb zircon study. *Geochimica et Cosmochimica Acta* 61:1531–1540.

Gibson R. L., Riemold W. U., Ashley A. J., and Koeberl C. 2002. Metamorphism on the Moon: A terrestrial analogue in the Vrederfort dome, South Africa? *Geology* 30:475–478.

Glass B. P. and Liu S. 2001. Discovery of high-pressure $ZrSiO_4$ polymorph in naturally occurring shock-metamorphosed zircons. *Geology* 29:371–373.

Goodrich C. A., Taylor G. J., Keil K., Kallemeyn G. W., and Warren P. H. 1986. Alkali norite, troctolites and VHK mare basalts from breccia 14304. Proceedings, 16th Lunar and Planetary Science Conference. pp. D305–D318.

Grange M. L., Nemchin A. A., Pidgeon R. T., Timms N., Muhling J. R., and Kennedy A. K. 2009. Thermal history recorded by the Apollo 17 impact melt breccia 73217. *Geochimica et Cosmochimica Acta* 73:3093–3107.

Grange M. L., Nemchin A. A., Timms N., Pidgeon R. T., and Meyer C. 2011. Complex magmatic and impact history prior to 4.1 Ga recorded in zircon from Apollo 17 South Massif aphanitic breccia 73235. *Geochimica et Cosmochimica Acta* 75:2213–2232.

Grange M. L., Pidgeon R. T., Nemchin A. A., Timms N. E., and Meyer C. 2013a. Interpreting U-Pb data from primary and secondary features in lunar zircon. *Geochimica et Cosmochimica Acta* 101:112–132.

Grange M. L., Nemchin A. A., and Pidgeon R. T. 2013b. The effect of 1.9 and 1.4 Ga impact events on 4.3 Ga zircon and phosphate from an Apollo 15 melt breccia. *Journal of Geophysical Research: Planets* 118:2180–2197.

Hartmann W. K. 1975. Lunar "cataclysm": A misconception? *Icarus* 24:181–187.

Hartmann W. K. 2003. Megaregolith evolution and cratering cataclysm models—Lunar cataclysm as a misconception (28 years later). *Meteoritics & Planetary Science* 38:579–593.

Hazen R. M. and Finger L. W. 1979. Crystal structure and compressibility of zircon at high pressure. *American Mineralogist* 64:196–201.

Head J. W., Fassett C. I., Kadish S. J., Smith D. E., Zurber M. T., Neumann G. A., and Mazarico E. 2010. Global distribution of large lunar craters: Implications for resurfacing and impactor populations. *Science* 329:1504–1507.

Hinton R. W. and Meyer C. 1991. Ion probe analysis of zircon and yttrobetafite in a lunar granite. Proceedings, 22nd Lunar and Planetary Science Conference. pp. 575–576.

Hopkins M. D. and Mojzsis S. J. 2015. A protracted timeline for lunar bombardment from mineral chemistry, Ti thermometry and U-Pb geochronology of Apollo 14 melt breccia zircons. *Contributions to Mineralogy and Petrology* 169:18.

Hudgins J. A., Spray J. G., Kelley S. P., Korotev R. L., and Sherlock S. C. 2008. A laser probe 40Ar/39Ar and INAA investigation of four Apollo granulitic breccias. *Geochimica et Cosmochimica Acta* 72:5781–5798.

Kamo S. L., Reimold W. U., Krough T. E., and Colliston W. P. 1996. A 2.023 Ga age for the Vrederfort impact event and a first report of shock metamorphosed zircons in pseudotachylitic breccias and Granophyre. *Earth and Planetary Science Letters* 144:369–387.

Krogh T. E., Davis D. W., and Corfu F. 1984. Precise U-Pb zircon and baddeleyite ages for the Sudbury area. In *The geology and ore deposits of the Sudbury structure*, edited by Pye E. G., Naldrett A. J., and Giblin P. E. *Ontario Geological Survey Special* 1:421–446.

Krogh T. E., Kamo S. L., Sharpton V. L., Marin L. E., and Hildebrands A. R. 1993. U-Pb ages of single shocked zircons linking distal K/T ejecta to the Chicxulub crater. *Nature* 366:731–734.

Lenz C. and Nasdala L. 2015. A photoluminescence study of REE^{3+} emissions in radiation-damaged zircon. *American Mineralogist* 100:1123–1133.

Leroux H., Reimold W. U., Koeberl C., Hornemann U., and Doukhan J. C. 1999. Experimental shock deformation in zircon: A transmission electron microscopic study. *Earth and Planetary Science Letters* 169:291–301.

Liu D., Jolliff B. L., Zeigler R. A., Korotev R. L., Wan Y., Xie H., Zhang Y., Dong C., and Wang W. 2012. Comparative zircon U-Pb geochronology of impact melt breccias from Apollo 12 and lunar meteorite SaU 169, and implications for the age of the Imbrium impact. *Earth and Planetary Science Letters* 319–320:277–286.

Losiak A., Wilhelms D. E., Byrne C. J., Thaisen K. G., Weider S. Z., Kohout T., O'Sullivan K., and Kring D. A. 2009. A new lunar impact crater database (abstract #1532). 40th Lunar and Planetary Science Conference. CD-ROM.

McKay D. S., Heiken G. H., Taylor R. M., Clanton U. S., Morrison D. A., and Ladle G. H. 1972. Apollo 14 soils: Size distribution and particle types. Proceedings, 3rd Lunar Science Conference. pp. 983–994.

McLeod C. L., Brandon A. D., Fernandes V. A., Peslier A. H., Fritz J., Lapen T., Shafer J. T., Butcher A. R., and Irving A. J. 2016. Constraints on formation and evolution of the lunar crust from feldspathic granulitic breccias NWA 3163 and 4881. *Geochimica et Cosmochimica Acta* 187:350–375.

Meyer C., Williams I. S., and Compston W. 1996. Uranium-lead ages for lunar zircons: Evidence for a prolonged period of granophyre formation from 4.32 to 3.88 Ga. *Meteoritics & Planetary Science* 387:370–387.

Morozova I., Shieh S. R., Moser D., Barker I., and Hanchar J. M. 2017. Strength and deformation of zircon at crustal and mantle pressures. In *Microstructural geochronology; Planetary records down to atom scale*, edited by Moser D., Corfu F., Darling J., Reddy S. and Tait K. Hoboken, New Jersey: John Wiley & Sons. pp. 167–182.

Morris R. V. 1978. The surface exposure (maturity) of lunar soils: Some concepts and Is/FeO compilation. Proceedings,

9th Lunar and Planetary Science Conference. pp. 2287–2297.

Moser D. E. 1997. Dating the shock wave and thermal imprint of the giant Vrederfort impact, South Africa. *Geology* 25:7–10.

Moser D. E., Cupelli C. L., Barker I. R., Flowers R. M., Bowman J. R., Wooden J., and Hart J. R. 2011. New zircon shock phenomena and their use for dating and reconstruction of large impact structures revealed by electron nanobeam (EBSD, CL, EDS) and isotopic U-Pb and (U-Th)/He analysis of the Vredefort dome. *Canadian Journal of Earth Science* 48:117–139.

Murakami T., Chakoumakos B. C., Ewing R. C., Lumpkin G. R., and Weber W. J. 1991. Alpha-decay event damage in zircon. *American Mineralogist* 76:1510–1532.

Nemchin A. A., Whitehouse M. J., Pidgeon R. T., and Meyer C. 2006. Oxygen isotopic signature of 4.4-3.9 Ga zircons as a monitor of differentiation processes on the Moon. *Geochimica et Cosmochimica Acta* 70:1864–1872.

Nemchin A. A., Pidgeon R. T., Whitehouse M. J., Vaughan J. P., and Meyer C. 2008. SIMS U-Pb study of zircon from Apollo 14 and 17 breccias: Implications for the evolution of lunar KREEP. *Geochimica et Cosmochimica Acta* 72:668–689.

Nemchin A. A., Pidgeon R. T., Healy D., Grange M. L., Whitehouse M. J., and Vaughan J. 2009a. The comparative behavior of apatite-zircon U-Pb systems in Apollo 14 breccias: Implications for the thermal history of the Fra Mauro formation. *Meteoritics & Planetary Science* 44:1717–1734.

Nemchin A. A., Timms N., Pidgeon R., Geisler T., Reddy S., and Meyer C. 2009b. Timing of crystallization of the lunar magma ocean constrained by the oldest zircon. *Nature Geoscience* 2:133–136.

Neumann G. A., Zuber M. T., Wieczorek M. A., Head J. W., Baker D. M. H., Solomon S. C., Smith D. E., Lemoine F. G., Mazarico E., Sabaka T. J., Goossens S. J., Melosh H. J., Phillips R. J., Asmar S. W., Konopliv A. S., Williams J. G., Sori M. M., Soderblom J. M., Milijkovic K., Andrews-Hanna J. C., Nimmo F., and Kiefer W. S. 2015. Lunar impact basins reveled by Gravity Recovery and Interior Laboratory measurements. *Sciences Advances* 1:9.

Norman M. D. and Nemchin A. A. 2014. A 4.2 billion year old impact basin on the Moon: U-Pb dating of zirconolite and apatite in lunar melt rock 67955. *Earth and Planetary Science Letters* 388:387–398.

Pidgeon R. T. 2014. Zircon radiation damage ages. *Chemical Geology* 367:13–22.

Pidgeon R. T., Nemchin A. A., Van Bronswijk W., Geisler T., Meyer C., Compston W., and Williams I. S. 2007. Complex history of a zircon aggregate from lunar breccia 73235. *Geochimica et Cosmochimica Acta* 71:1370–1381.

Pidgeon R. T., Merle R. E., Grange M. L., Nemchin A. A., and Whitehouse M. J. 2016. Annealing of radiation damage in zircons from Apollo 14 impact breccia 14311: Implications for the thermal history of the breccia. *Meteoritics & Planetary Science* 51:155–166.

Pope K. O., Kieffer S. W., and Ames D. E. 2004. Empirical and theoretical comparisons of the Chicxulub and Sudbury impact structures. *Meteoritics & Planetary Science* 39:97–116.

Reddy S. M., Timms N. E., Pantleon W., and Trimby P. 2007. Quantitative characterization of plastic deformation of zircon and geological implications. *Contributions to Mineralogy and Petrology* 153:625–645.

Reimold W. U. and Gibson R. L. 1996. Geology and evolution of the Vrederfort impact structure, South Africa. *Journal of African Earth Sciences* 23:125–162.

Reimold W. U., Leroux H., and Gibson R. L. 2002. Shocked and thermally metamorphosed zircon from the Vrederfort impact structure, South Africa. *European Journal of Mineralogy* 15:859–868.

Ryder G. 1990. Lunar samples, lunar accretion and the Earth bombardment of the Moon. *Eos* 71:313, 322–323.

Schaeffer A. and Husain L. 1973. Early lunar history: Ages of 2 to 4 mm soil fragments from the lunar highlands. *Geochimica et Cosmochimica Acta Supplement* 4:1847–1863.

Smith J. M., Meyer C., Compston W., and Williams I. S. 1986. 73235,82 (pomegranate): An assemblage of lunar zircon with unique overgrowth. Proceedings, 17th Lunar and Planetary Science Conference. pp. 805–806.

Stöffler D. and Hornemann U. 1972. Quartz and feldspar glasses produced by natural and experimental shock. *Meteoritics & Planetary Science* 7:371–394.

Stöffler D., and Langenhorst F. 1994. Shock metamorphism of quartz in nature and experiment: I. Basic observation and theory. *Meteoritics & Planetary Science* 29:155–181.

Swann G. A. Bailey N. G., Batson R. M., Eggleton R. E., Hait M. H., Holt H. E., Larson K. B., Reed V. S., Schaber G. G., Sutton R. L., Trask N. J., Ulrich G. E., and Wilshire H. G. 1977. *Geology of the Apollo 14 landing site in the Fra Mauro Highlands*. U.S. Geological Survey Professional Paper 888. Washington, D.C.: United States Government Printing Office. 103 p.

Taylor D. J., McKeegan K. D., and Harrison T. M. 2009. Lu-Hf zircon evidence for rapid lunar differentiation. *Earth and Planetary Science Letters* 279:157–164.

Tera F., Papanastassiou D. A., and Wasserburg G. J. 1974. Isotopic evidence for a terminal lunar cataclysm. *Earth and Planetary Science Letters* 22:1–21.

Timms N. E., Reddy S. M., Healy D., Nemchin A. A., Grange M. L., Pidgeon R. T., and Hart R. 2012. Resolution of impact-related microstructures in lunar zircon: A shock-deformation mechanism map. *Meteoritics & Planetary Science* 47:120–141.

Timms N. E., Erickson T. M., Pearce M. A., Cavosie A. J., Tohver E., Reddy S. M., Zanetti M. R., Nemchin A. A., and Wittmann A. 2017. A pressure-temperature phase diagram for zircon at extreme conditions. *Earth-Science Reviews* 165:185–202.

Timms N. E., Healy D., Erickson T. M., Nemchin A. A., Pearce M. A., and Cavosie A. J. 2018. Role of elastic anisotropy in the development of deformation microstructures in zircon. In *Microstructural geochronology: Planetary records down to atom scale*, edited by Moser D., Corfu F., Darling J., Reddy S., and Tait K. Hoboken, New Jersey: John Wiley & Sons. pp. 183–202.

Tsuchiya Y., Kayama M., Nishido H., and Noumi Y. 2015. Annealing effects on cathodoluminescence of zircon. *Journal of Mineralogical and Petrological Sciences* 110:283–292.

Turner G., Cadogan P. H., and Yonge C. J. 1973. Argon selenochronology. *Geochimica et Cosmochimica Acta Supplement* 4:1889–1914.

Weber W. J. 1990. Radiation-induced defects and amorphization in zircon. *Journal of Material Research* 5:2687–2697.

Weber W. J., Ewing R. C., and Wang L.-M. 1994. The radiation-induced crystalline to amorphous transition in zircon. *Journal of Material Research* 9:688–698.

Wilhelms D. E. 1987. *The geologic history of the Moon*. U.S. Geological Society Survey Professional Paper 1348. Washington, D.C.: United States Government Printing Office. 302 p.

Wilshire H. G. and Jackson E. D. 1972. *Petrology and stratigraphy of the Fra Mauro Formation at the Apollo 14 site*. U.S. Geological Survey Professional Paper 785. Washington, D.C.: United States Government Printing Office. 26 p.

Wittmann A., Kenkmann T., Schmitt R. T., and Stoffler D. 2006. Shock-metamorphosed zircon in terrestrial impact craters. *Meteoritics & Planetary Science* 41:433–454.

Zhang A.-C., Hsu W.-W., Li X.-H., Ming H.-L., Li Q.-L., Liu Y., and Tang G.-Q. 2011. Impact melting of lunar meteorite Dhofar 548: Evidence from polycrystalline texture and decomposition of zircon. *Meteoritics & Planetary Science* 46:103–115.

Zhang M., Salje K. K. H., Farnan I., Graeme-Barber A., Daniel P., Weing R. C., Clark A. M., and Leroux H. 2000. *Journal of Physics: Condensed Matter* 12:1915–1925.

SUPPORTING INFORMATION

Additional supporting information may be found in the online version of this article:

Table S1. Previously reported lunar zircon microstructures, EBSD analytical parameters, and summary of terrestrial impact craters discussed in manuscript.

Data S2. Electron beam images and descriptions of all lunar zircons in study.

Fig. S1. Lunar nearside with locations of Apollo landing sites and lunar basins (>300 km) identified in GRAIL gravity anomaly map (modified from Neumann et al. 2015).